Fusing Landsat and SAR data for mapping tropical deforestation through machine learning classification and the PVts-β non-seasonal detection approach

Fusion des données Landsat et SAR pour la cartographie de la déforestation tropicale grâce à la classification par apprentissage automatique et à l'approche de détection non saisonnière PVts-β

Yonatan Tarazona[a,e]*, Alaitz Zabala[b], Xavier Pons[b], Antoni Broquetas[a], Jakub Nowosad[c], Hamdi A. Zurqani[d]

[a]*Department of Signal Theory and Communications, School of Telecommunication Engineering, Universitat Politecnica de Catalunya, 08034 Barcelona, Spain*

[b]*Grumets Research Group, Dep. Geografia, Edifici B, Universitat Autònoma de Barcelona, Bellaterra, 08193 Catalonia, Spain*

[c]*Institute of Geoecology and Geoinformation, Adam Mickiewicz University, Krygowskiego 10, 61-680, Poznan, Poland*

[d]*Department of Forestry and Environmental Conservation, Clemson University, SC, USA*

[e]*American Program in GIS and Remote Sensing, Peru*

[a,e]*geoyons@gmail.com, [b]alaitz.zabala@uab.cat, [b]xavier.pons@uab.cat,*

[a]*broquetas@tsc.upc.edu, [c]nowosad.jakub@gmail.com, [d]hzurqan@clemson.edu*

Fusing Landsat and SAR data for mapping tropical deforestation through machine learning classification and the PVts-β non-seasonal detection approach

ABSTRACT

This article focuses on mapping tropical deforestation using time series and machine learning algorithms. Before detecting changes in the time series, we reduced seasonality using Photosynthetic Vegetation (PV) index fractions obtained from Landsat images. Single and multi-temporal filters were used to reduce speckle noise from Synthetic Aperture Radar (SAR) images (i.e., ALOS PALSAR and Sentinel-1B) before fusing them with optical images through Principal Component Analysis (PCA). We detected only one change in the two PV series using a non-seasonal detection approach, as well as in the fused images through five machine learning algorithms that were calibrated with Cross-Validation (CV) and Monte Carlo Cross Validation (MCCV). In total, four categories were obtained: forest, cropland, bare soil and water. We then compared the change map obtained with time series and that obtained with the classification algorithms with the best calibration performance, revealing an overall accuracy of 92.91% and 91.82% respectively. For statistical comparisons we used deforestation reference data. Finally, we conclude with some discussions and reflections on the advantages and disadvantages of the detections made with time series and machine learning algorithms, as well as the contribution of SAR images to the classifications, among other aspects.

RÉSUMÉ

Cet article porte sur la cartographie de la déforestation tropicale à l'aide de séries chronologiques et d'algorithmes d'apprentissage automatique. Avant de détecter les changements dans les séries temporelles, nous avons réduit la saisonnalité en utilisant les fractions de l'indice de végétation photosynthétique (PV) obtenues à partir des images Landsat. Des filtres mono- et multi-temporels ont été utilisés pour réduire le bruit de chatoiement des images SAR (Synthetic Aperture Radar) (c'est-à-dire ALOS PALSAR et Sentinel-1B) avant de les fusionner avec les images optiques par le biais de l'analyse en composantes principales (ACP). Nous avons détecté un seul changement à la fois dans les séries de PV en utilisant une approche de détection non saisonnière, ainsi que dans les images fusionnées, grâce à cinq algorithmes d'apprentissage automatique qui ont été calibrés par validation croisée (CV) et validation croisée de Monte Carlo (MCCV). Au total, quatre catégories ont été obtenues : forêt, terres cultivées, sol nu et eau. Ensuite, nous avons comparé

la carte des changements obtenue avec les séries temporelles et celle obtenue avec les algorithmes de classification les plus performants en matière de calibration, révélant une précision globale de 92,91% et 91,82% respectivement. Pour les comparaisons statistiques, nous avons utilisé des données de référence sur la déforestation. Enfin, nous concluons par quelques discussions et réflexions sur les avantages et les inconvénients des détections effectuées avec les séries temporelles et les algorithmes d'apprentissage automatique, ainsi que sur la contribution des images SAR dans les classifications, entre autres aspects.

Introduction

Deforestation resulting from anthropogenic activities, and defined as conversion of forest to another land use, as well as the long-term reduction of the tree canopy cover below the minimum 10 percent threshold (FAO 2018), have had a significant impact on terrestrial biodiversity and productivity all over the World. In fact, forest change is one of the major processes of global land-cover change (Ding et al. 2019). Forests play a crucial role in ecosystem services, including carbon sequestration, climate and water cycle regulation, and maintenance of biodiversity (Gibson et al. 2011; Turubanova et al. 2018). In particular, tropical regions have been undergoing rapid changes in forest cover mainly due to land-use change. For example, tropical deforestation accounts for 10%–15% of anthropogenic greenhouse gas emissions (Houghton 2013). Tropical deforestation has been occurring since the 1980s (van der Werf et al. 2009; Achard et al. 2010; Hansen et al. 2013; Achard et al. 2014) and threatens biodiversity, ecosystem services and water security on the planet.

Remote sensing has played a key role in studying the environment, especially since the launch of Landsat-1 in 1972 (Vidal-Macua et al. 2017). Free and open access to the Landsat archive has dramatically benefited operational applications, scientific studies, and discoveries based on analyses of large numbers of Landsat images (Zhu et al. 2019). For example, annual forest change has been globally mapped using available Landsat observations from 2000 to 2012. This global mapping reports a net deforestation of 1.5 million km2 worldwide (Hansen et al. 2013). Several approaches, which can exploit the full temporal detail of available archives, have been proposed to map tropical deforestation from local to global scales (e.g., Souza et al. 2005; Asner et al. 2009; Kennedy et al. 2010; Verbesselt et al. 2012; Hansen et al. 2013; Zhu and Woodcock 2014). However, and according to Tarazona et al. (2018), the main limitations of most of the detection algorithms based on time-series, such as Breaks For Additive Season and Trend (BFAST) (Verbesselt et al. 2010) or Continuous Change Detection and Classification (CCDC) (Zhu and Woodcock 2014), are: i) they have different and excessive calibration parameters that hinder the process of effective and rapid

monitoring of deforestation events; and (ii) they depend heavily on seasonality in the time series. To address these limitations, Tarazona et al. (2018) proposed a novel detection approach called PVts-β, which has one calibration parameter and detections that are not dependent on the seasonal component of the time series.

However, in tropical regions cloud cover seriously affects the possibilities of adequately mapping deforestation (Zhu et al. 2019), and some tropical countries have cloud cover that exceeds the long-term yearly average frequency of 80%. Persistent cloud cover inhibits full optical coverage from Landsat-like sensors even when compositing is performed over a period of 1 to 2 years (Souza et al. 2013). Synthetic Aperture Radar (SAR) can penetrate clouds, and therefore has the potential of complementing optical-based forest monitoring systems (Joshi et al. 2016). Several authors have used these images to map deforestation (e.g., Park and Chi 2008; Trisasongko 2010; Jia and Wang 2018). Since Advanced Land Observing Satellite (ALOS) Phased Arrayed L-band Synthetic Aperture Radar (PALSAR) data have become freely available and with the launch of the Sentinel-1A and 1B C-band SAR satellites in 2014 and 2016 (Torres et al. 2012), for the first time, dense SAR time series are free and openly available for the tropical region. Nevertheless, shorter wavelength C-band (~5.5 cm) SAR is generally less useful for monitoring forest change due to the lower penetration depth and rapid saturation of the signal over forests (Woodhouse 2005). However, the high temporal observation density of the Sentinel-1 C-band compensates for the low sensitivity for detecting deforestation, when compared to longer wavelength L-band (e.g., ALOS PALSAR) SAR observations (Reiche et al. 2018). The main negative aspect of SAR images is speckle noise, which impoverishes radiometric resolution and affects interpretation and classification results. Reducing speckle-noise leads to a decrease in spatial resolution, and therefore reduces the potential of these images for coverage analyses.

Multi-sensor data fusion approaches (Zhang 2010) combining SAR and Landsat optical sensors have demonstrated a clear increase in forest mapping accuracy. This is mainly because fusing the

different data enhances visual interpretation and also improves the performance of quantitative analyses. Furthermore, in recent years there have been significant advances in techniques for fusing SAR with optical data, such as the wavelet-merging technique (Hong and Zhang 2008; Lu et al. 2011; Abdikan 2016), Principal Component Analysis (PCA) (Walker et al. 2010; Pereira et al. 2013; Abdikan 2016) and intensity-hue-saturation (IHS) (Abdikan 2016). However, there is still no consensus in the scientific community on the best method for integrating SAR and optical data for mapping the effects of deforestation, especially in tropical forests (Pereira et al. 2013). Approaches that combine optical and SAR time series imagery to detect deforestation must overcome various challenges, including accurate co-registration and speckle noise, among others.

In this study, we propose detecting deforestation in a tropical region in south-eastern Peru using only optical data (Landsat 5 Thematic Mapper (TM) and Landsat 8 Operational Land Imager (OLI)), and combining optical data and SAR data, i.e. only two dates. An optical and radar image for each date was used for the data fusion. For the first case, we used long series of Photosynthetic Vegetation (PV) index fractions in order to reduce seasonality in the time series. These PV fractions were obtained from the Carnegie Landsat Systems Analysis-Lite (CLASlite) program (Asner et al. 2009) under an Automated Monte Carlo Unmixing approach (AutoMCU), which provides quantitative analysis of the fractional or percentage cover (0-100%) of live vegetation. In the second case, the PCA method was used for data fusion, which does not lead to a loss in spatial resolution (i.e., it does not perform smoothing) and makes it possible to obtain the contribution (%) of the variables in the fusion. Therefore, our objectives address: (i) to detect changes in the Peruvian rainforest between 2009 and 2018 (i.e., obtain a single change map) using the PVts-β approach through PV series, (ii) to detect changes using machine learning algorithms with the fused images for the same period as in the previous case, (iii) to evaluate the change maps obtained with the PVts-β approach and the fused images, and (iv) to discuss the main advantages and disadvantages

of detections based on time series and machine learning, as well as the benefits of the contributions of SAR images to classifications and change detections.

Study area

Our study area is located in Madre de Dios, a region in the southeast of Peru (see Fig. 1). Madre de Dios has a flat topography, with a minimum and maximum altitude of 170 and 360 masl (meters above sea level). This moderate slope facilitates the co-registration process between optical and SAR images. The study area is included in path/row 003/069 within the World Reference System-2 (WRS-2) and covers approximately 1100x1100 Landsat pixels (i.e., $\approx$ 1090km2). Madre de Dios is a hotspot of great biodiversity (Tarazona and Miyasiro-López 2020) and 40% of its area is protected by a set of Protected Natural Areas and Native Communities. It also has the largest coal reserves in the world (Baccini et al. 2012). However, deforestation that occurs in the region, based mainly on logging, agriculture and gold mining (Fig. 1c), is endangering forest ecosystem services and having negative effects on the surrounding population and the Peruvian state. In fact, the latest reports of deforestation, made by the Peruvian state through the national reports of the Ministry of the Environment of Peru (MINAM), indicate an increase in deforestation in recent years.

Fig. 1. Political map (panel (a)) and Madre de Dios study area with a Landsat 8 OLI background image in RGB combination: SWIR2, SWIR1 and GREEN bands (panel (b)). Panel (d) shows the Digital Elevation Model (DEM) of the Shuttle Radar Topographic Mission (SRTM), both panel (b) and panel (d) represent the same study area. Panel (c) shows gold mining through PlanetLabs images (at 5m); in addition, the resolution of this image makes it possible to see the characteristics of the gold mining in the study region (i.e., presence of water bodies).

Data and methods

We follow a series of rigorous processes according to the premise set out in the introduction (see Fig. 2). Section 3.1 details the pre-processing of optical images with the CLASlite software to obtain the PV fractions and a standard pre-processing of the SAR images that includes co-registration with optical images. Section 3.2 provides a review of the reference data used to evaluate the obtained maps. In section 3.3 we conducted a brief and highly focused review of the optical and SAR data fusion method used. Finally, in section 3.4 we include several techniques and standard guidelines for the mapping and validation of the change cartography.

Fig. 2. Flowchart of the pre-processing and processing of the optical and SAR images is shown.

Satellite image processing

Landsat data and fraction indices

In this study, 50 images from Landsat TM and OLI pairs between 1990 and 2018 with a Tier 1 processing level (Young et al. 2017) were selected. Exactly 38 images correspond to the TM sensor (1990-2011) and 12 to the OLI sensor (2013-2018). Photosynthetic Vegetation fractions were obtained from 50 reflectance images with the CLASlite software (Asner et al. 2009). In short, CLASlite uses the physical model Spectral Mixture Analysis (SMA) to obtain the PV fractions. SMA assumes that the energy received within the field of vision of the remote sensor can be considered as the sum of the energies received from each dominant endmember (specifically a Linear Mixing Model). Therefore, we would expect advantages in the detections because we are working with changes in photosynthetic activity at the subpixel level. Given the potential of CLASlite subpixel analysis, the AutoMCU approach has been widely used to map forest disturbance and deforestation worldwide (e.g., Asner et al. 2005, 2009; Carlson et al. 2012; Allnutt et al. 2013; Bryan et al. 2013; Dlamini 2017; Tarazona et al. 2018).

After obtaining the PV fractions we deal with the atmospheric artefacts using the Function of mask (Fmask) (Zhu and Woodcock 2012) to mask clouds and cloud shadows. Subsequently, and to generate cloud-free mosaics for each year, we used the algorithm proposed by Tarazona et al. (2018). This algorithm consists in three steps: i) it chooses the image less affected by atmospheric noise, retaining the image with the highest number of clear pixels and its acquisition time, ii) it calculates the distances (i.e., differences in acquisition time) of the image selected in step (i) to the remaining images, and iii) it takes the clean pixels of the images, starting with the image that has the shortest distance to the image selected in step (i) and ending with the image most temporally distant.

A total of 28 yearly PV fraction images was created (1990-2018 time series) (of a total of 50 images).

ALOS PALSAR and Sentinel-1 data

We used ALOS PALSAR data in Fine Beam dual Polarization (FBD) with Terrain Corrected for this study. The image was acquired on 12 August, 2009, with a spatial resolution of 12.5 m, swath of 70 km, in HH and HV-polarizations. Both polarizations were acquired in gamma-naught radar backscattering coefficients (γ^0) (Rosenqvist et al. 2007). We softened the salt and pepper effect by using a Simple Speckle Filter (SSF) through the Lee filter (Lee 1980) with a movable 3x3 window. We then converted it into decibels (dB) using the SNAP software (Sentinel Application Platform, see http://step.esa.int/main/download/) of the European Space Agency.

Sentinel-1 is a C-band Synthetic Aperture Radar (5.5cm wavelength) imaging mission (Torres et al. 2012) that supports a wide variety of applications, including deforestation assessment. Sentinel-1B with VV+VH polarization (S1B-VV+VH) data were acquired in Interferometric Wide Swath mode (IW with 250km swath). The S1B-VH+VV image was acquired on 22 December, 2018 and was downloaded in Ground Range Detected (GRD) format. The pre-processing was also performed with the SNAP software and consisted of three steps: (i) calibration, (ii) terrain correction, and (iii)

smoothing of speckle noise just as we did with ALOS PALSAR. For terrain correction we used the Range-Doppler Terrain Correction model and a three arc-second DEM obtained from the SRTM and downloaded automatically by the SNAP software. The spatial output resolution after applying the correction to the terrain was 10m. The VV and VH radar backscattering coefficients ($\sigma0$ in dB) were obtained from digital number (DN) values through Eq. 1:

$$dB_{i,j} = 10 * log_{10}(DN_{i,j}^{2}/A^{2}) \tag{1}$$

where, i, j represents the position (row and column), and A represents the calibration factor, which can be looked up in the sigma naught values in the lookup table (LUT).

In addition, accurate multi-temporal co-registration is an essential prerequisite for change detection and was also carried out with the SNAP software. The Optical Landsat (see section 3.3) image was selected as master and the SAR images as slaves, and a Root Mean Square Error (RMSE) accuracy threshold of 0.5 pixels was applied (i.e., 15m). The RMSE of the co-registration between the optical and SAR images for the two periods was less than 0.5 pixels (Table 1).

Table 1. Number of tie points, threshold of accuracy and RMSE in pixel units obtained after co-registration between optical and radar data.

	Fusion	Tie points	RMSE mean	RMSE std
2009	SWIR1 (master) + HH (slave)	457	0.18167	0.09060
	SWIR1 (master) + HV (slave)	489	0.16986	0.07929
2018	SWIR1 (master) + VV (slave)	568	0.24612	0.11843
	SWIR1 (master) + VH (slave)	566	0.24455	0.11167

*std: standard deviation

Deforestation reference data

In order to validate the detected deforestation events, two sources have been used as reference data (i.e., deforested areas and intact forest mask). First, we used the official deforestation reports from the Peruvian government carried out by the Ministry of the Environment (MINAM 2015) (see: http://geobosques.minam.gob.pe/geobosque/view/index.php for more details). The methodology of these reports is based on the work of Hansen et al. (2008) and Potapov et al. (2011). These reports show the deforestation between 2001 and 2017. Second, we used the global forest change data from Hansen et al. (2013), which were obtained from time-series analysis of Landsat images including the OLI sensor. These reports are open-access and are usually used as ground truth (global forest change between 2000 and 2018). We used the Google Earth Engine platform (Gorelick et al. 2017) to download them (see: https://earthenginepartners.appspot.com/science-2013-global-forest/download_v1.6.html for more details).

Fusion of SAR and optical images through PCA

To fuse optical (Landsat imagery) and SAR images (ALOS PALSAR and Sentinel-1) we used the PCA method that is widely known by the scientific community (e.g., Pereira et al. 2013; Werner et al. 2014; Abdikan 2016). The goal is to reduce the dimensionality through linear combinations of the original variables, obtaining the contribution of the optical bands and SAR in the principal components (PC). We believe that a description of the mathematical depth of the PCA is important for understanding the internal process of fusion of the two images with different observation geometries and which few studies have been able to develop; therefore, we present the mathematical description in Appendix A.

A total of nine variables (Z_i) are considered in the two periods. Specifically, six optical bands for both 2009 and 2018, two HH and HV polarizations for 2009, and another two VV and VH polarizations for 2018. In addition, we include the HH/HV and VV/VH ratios for 2009 and 2018,

respectively. The two ratios are effective in detecting deforestation and are correlated with forest phenology (e.g., Zeng et al. 2014 and Frison et al. 2018).

The Landsat images used for the fusion were selected to match the acquisition date of the SAR images as closely as possible. Therefore, 28 August, 2009 and 6 September, 2018 were selected from among the available optical images. To fuse the images we used the "fusionRS" function (see Appendix B for more details). This function uses the prcomp function embedded in R (R Core Team 2020) to execute the PCA. The outputs of the "fusionRS" function are the eigenvalues, eigenvectors, the correlation of the variables with the PC and the contribution in % of each variable in each PC in a user-friendly and straightforward way (all the documentation on how to execute the function and also examples can be found in Appendix B).

Moreover, given the nature of the SAR images and optical images, all variables were centred and scaled (i.e., standardized) (Eq. 2) before computing the PCA to prevent any variable from having a disproportionate influence on the PCA.

$$Z = \frac{x - \mu}{\sigma} \tag{2}$$

Where, x is the original variable, μ is the mean, σ the standard deviation of the original variables and Z is the standardized variable.

Mapping deforestation

Non-seasonal detection approach

Time series methods for mapping deforestation are generally classified into seasonal and non-seasonal approaches. Seasonal approaches are widely used and a variety of algorithms have been proposed (e.g., those proposed by Verbesselt et al. 2012 or Zhu and Woodcock 2014), but all of them are highly dependent on the seasonal component of the time series. As a result of this dependence, they have a number of shortcomings that make it difficult to map changes in the forest

quickly and accurately. However, the non-seasonal approach (e.g., PVts-β proposed by Tarazona et al. (2018)), does not depend on seasonality and detections may be more accurate than the others.

Therefore, we used the PVts-β approach proposed to detect deforestation between 2009 and 2018. For this, we used series of PV fractions to minimize the effect of seasonality and improve detection accuracy. This approach consists of a series of processes that are detailed in the work of Tarazona et al. (2018). The optimal threshold values (β) (Eq. 3) are 5 and 6 for PV series. In this work we used the value β=5.

$$L_{i,j} = \mu_{i,j} - \beta * \sigma_{i,j} \tag{3}$$

Where, $L_{i,j}$ is the lower limit, $\mu_{i,j}$ is the mean, $\sigma_{i,j}$ is the standard deviation, β is the threshold magnitude and i, j is the row and column position of a given pixel.

For example, Fig. 3 shows two time series of the PV fraction for pixels where the forest is deforested. Fig. 3a shows a deforestation event due to agricultural activity in 2011, and Fig. 3b shows another deforested area in 2010, caused by gold mining activity, which has a large negative impact on the environment.

Fig. 3. Examples of time series of forests that have been deforested (points in blue). The Landsat images in the top row are in combination SWIR2, NIR and RED. The middle row contains the PV fractions scaled between 0 and 100. Finally, the lower row shows the detections made by the PVts-β approach with β=5. The PV series were smoothed, before detecting deforestation, with the "smootH" function (see Appendix B).

Classification methods

After applying PCA to fuse the images, five popular robust machine learning algorithms in R language were used to detect changes. Support Vector Machine (SVM) was the first algorithm

13

used. The SVM classifier is a supervised non-parametric statistical learning technique that does not assume a preliminary distribution of input data (Mountrakis et al. 2011; Pôssa and Maillard 2018). Its discrimination criterion is a hyperplane that separates the classes in the multidimensional space in which the samples that have established the same classes are located, generally some training areas. The SVM classifier has been efficiently used for mapping vegetation and forest (Knorn et al. 2009; Duro et al. 2012). The second algorithm used was Random Forest (RF). RF is a derivative of Decision Tree which provides an improvement over DT to overcome the weaknesses of a single DT (Pal 2005; He et al. 2017; Vlachopoulos et al. 2020). The prediction model of the RF classifier only requires two parameters to be identified: the number of classification trees desired, known as "ntree", and the number of prediction variables, known as "mtry", used in each node to make the tree grow (Rodriguez-Galiano et al. 2012). The third algorithm used was Decision Tree (DT). DT is also a supervised non-parametric statistical learning technique, where the input data is divided recursively into branches (Chen et al. 2019) depending on certain decision thresholds until the data are segmented into homogeneous subgroups. This technique has substantial advantages for remote sensing classification problems due to its flexibility, intuitive simplicity, and computational efficiency (Friedl and Brodley 1997). The fourth algorithm used was Naive Bayes (NB). The NB classifier is an effective and simple method for image classification based on probability theory. The NB classifier assumes an underlying probabilistic model and captures the uncertainty about the model in a principled way, i.e. by calculating the occurrence probabilities of different attribute values for different classes in a training set (Pradhan et al. 2010). The last algorithm used was Neuronal Networks (NN). This classification consists of a neural network that is organized into several layers, i.e., an input layer of predictor variables, one or more layers of hidden nodes, in which each node represents an activation function acting on a weighted input of the previous layers' outputs, and an output layer (Liu et al. 2019).

The fine-tuning of model hyperparameters can significantly increase the target in both training and testing; however, it also increases the cost of training models and the risk of overfitting. Therefore, in this research we decided to use the default parameters (see S1 in supplementary material) after examining a large number of studies (Belgiu and Drăguţ 2016; Tyralis et al. 2019; Zurqani et al. 2019).

Since our study area is located in the Amazon, obviously the classes to be identified were mainly forest, cropland, bare soil and water. Classification of crop types or differentiating secondary forests from virgin forests will not be addressed in this study due to the nature and objectives of the research. The objective is to separate forest from other classes.

Calibration

Undoubtedly, given the large number of machine learning algorithms, it was necessary to select the one with the best performance in the classification, i.e. the algorithm in which the training and testing data used converge the learning iteratively to a solution that appears to be satisfactory. Therefore, calibration at this stage was crucial and was carried out through Cross-Validation (CV) and Monte Carlo Cross-Validation (MCCV). We used k groups equal to 10 (10 iteration) and an iteration equal to 100 for CV and MCCV respectively. In order to select the best classifier, which will then serve as input for the 2009 and 2018 classifications, it was necessary to minimize the testing bias (the mean of errors $e_i = 1 - overall\ accuracy$) (Eq. 4) and the testing variance (the standard deviation of errors e_i) (Eq. 5) so that the model works well for both the training data and the test data. This process and analysis was written in R with the help of some libraries, such as caret and willcoxCV.

$$bias = \sum_{i=1}^{n} e_i/n \qquad\qquad (4)$$

$$variance = \sqrt{\sum_{i=1}^{n} \left(e_i - \underline{e}\right)^2/n} \qquad\qquad (5)$$

Where, i represents the position of a specific iteration and n represents the total number of iterations executed.

Accuracy assessment and map comparison

A total of 1670 training points were taken to calibrate and validate the different cartographic products generated (Table 2). These points were selected through the interpretation of the satellite images themselves, truth-terrain reference data elaborated by MINAM (2015) and, on some occasions, we used high-resolution images such as Google Earth. First, we selected 560 points for the calibration of the five classifiers for each of the two years, 2009 and 2018, through a stratified random sampling approach (Olofsson et al. 2014). These same points were also used to obtain the definitive 2009 and 2018 class maps using the classifier with the best performance. In both periods, the 560 points were split into training (60%) and testing (40%) sets through proportional stratified random sampling. Finally, to validate the change map generated with the classifiers and the changes with the PVts-β approach, we selected 550 points using stratified random sampling (80% for intact forest and the rest for deforested areas).

Table 2. Number of points for the calibration of the classifiers and also for obtaining the change cartography for the years 2009 and 2018, as well as samples for validating the changes obtained with the classifiers and the PVts-β approach.

| | | Calibration | | Change validation |
		Year 2009	Year 2018	
	Forest	225	225	Training
	Cropland	125	125	336
Classifiers	Bare soil	105	105	Testing
	Water	105	105	224
	Total	560	560	560

Change maps	
	550
PVts-β approach	

To evaluate the accuracy of both the image fusion classifications and the detections of the PVts-β approach, we used indicators such as overall accuracy, user's accuracy, producer's accuracy and kappa index (Congalton and Green 2008). These indicators have been widely discussed and used in a large number of papers, such as Schultz et al. (2016) and Duro et al. (2012), among others.

Fig. 4. Panel (a) and (b) show the combinations NIR, RED and GREEN and SWIR2, SWIR1, GREEN from the year 2009 (Landsat-5 TM). Panel (c) and (d) show the same region with polarizations HH and HV (ALOS PALSAR - 2009) respectively. Panel (e) and (f) show the combinations NIR, RED and GREEN and SWIR2, SWIR1, GREEN from the year 2018 (Landsat-8 OLI). Panel (g) and (h) show the same region with polarizations VV and VH (Sentinel 1B - 2018). Finally, panel (i) and (j) show the fused images of 2009 and 2018 respectively, in both cases using a combination with the first three principal components.

Results
Fusion of optical and SAR images

The fusions of optical and SAR data for the years 2009 and 2018 are shown in Fig. 4(a-h). In both panels, they are shown in a 1-2-3 combination of 9 principal components (Fig. 4i-j). Only the first principal components provided the greatest variance in explaining the data in both 2009 and 2018 (Fig. 5). At this stage we used the jambu elbow (Tibshirani et al., 2001) to decide which components to take out of the equation due to the poor contribution to the variance. In fact, for 2009 and 2018, only the six and five principal components had an accumulated variance of 98.96% and 99.44% respectively (Fig. 5). In addition, increasing the number of principal components would bring us closer to a context of using almost all the variables involved and an increase in noise,

17

which could ultimately hinder the classification process through automatic learning algorithms.

Fig. 5. Proportion of variance of each PC and the cumulative variance for the year 2009 is shown in panel (a); panel (b) shows the same for the year 2018.

On the other hand, Table 3 shows the contributions (%) of the original variables to the principal components. In general, for the year 2009 almost all optical bands had a significant contribution in PC1 (except NIR band), the NIR and SWIR1 bands in PC2:3, all bands in PC4 (except SWIR2), all (except RED and NIR bands) in PC5 and the NIR, SWIR1 and SWIR2 bands in PC6. While all polarizations had a strong contribution in all PC1:6 (except HH in PC1, HH/HV in PC2 and PC6, HV in PC3 and HH in PC6). In addition, it is important to note that, of all the SAR bands, the HV polarization had the largest contribution in PC1, followed by HH/HV. For 2018, the behaviour is quite similar. Like 2009, almost all optical bands made a large contribution in PC1 (except NIR band), NIR, SWIR1 and SWIR2 bands in PC2, RED, NIR and SWIR1 in PC3, all bands in PC4 and all bands (except SWIR1 and SWIR2) in PC5. While all polarizations, especially VH and VV, had a significant contribution in PC1:5, with the exception of PC4.

Table 3. Contribution in percentages (%) of the variables to the principal components after the fusion of optical and SAR images for the years 2009 and 2018. Lower contributions in each PC are shown in red and blue for optical and radar bands respectively. The last PC that will not be used in the classification are shown in grey.

Contributions (%)								
Year 2009								
PC1	PC2	PC3	PC4	PC5	PC6	PC7	PC8	PC9

	PC1	PC2	PC3	PC4	PC5	PC6	PC7	PC8	PC9
Proportion of Variance (%)	48.601	21.013	10.806	8.067	5.890	4.579	0.722	0.286	0.035
BLUE	20.017	0.641	0.053	7.611	2.763	5.132	56.201	0.000	7.945
GREEN	21.138	0.204	0.061	6.675	2.370	2.780	2.486	1.194	63.212
RED	20.618	1.015	0.369	7.844	1.656	0.183	38.885	1.498	28.332
NIR	0.409	34.911	8.292	7.437	1.304	37.021	1.351	8.363	0.344
SWIR1	9.507	17.939	3.343	8.973	5.077	10.057	0.984	42.521	0.058
SWIR2	17.963	1.647	0.208	0.574	4.488	27.996	0.009	46.417	0.106
HH	1.725	18.939	35.887	15.133	27.235	2.118	0.002	0.001	0.000
HV	5.402	23.393	2.858	5.995	49.887	14.039	0.078	0.000	0.000
HH/HV	3.216	1.305	48.925	39.755	5.216	0.670	0.000	0.002	0.000

Year 2018

	PC1	PC2	PC3	PC4	PC5	PC6	PC7	PC8	PC9
Proportion of Variance (%)	57.723	21.485	9.650	6.618	3.964	0.339	0.103	0.089	0.029
BLUE	16.698	0.772	1.568	8.781	9.807	53.780	0.200	0.001	8.389
GREEN	17.618	0.375	1.715	5.779	7.148	2.609	0.018	1.728	63.006
RED	17.816	0.125	2.151	2.780	6.491	41.863	0.163	0.547	28.058
NIR	0.382	28.121	17.701	40.529	11.477	0.547	0.117	1.100	0.021
SWIR1	7.373	22.559	4.034	22.293	2.661	0.388	3.596	36.929	0.163
SWIR2	12.684	11.431	0.357	18.788	0.110	0.008	3.052	53.207	0.358
VV	11.513	16.100	5.491	0.220	10.170	0.094	52.850	3.555	0.001
VH	12.173	5.548	9.535	0.500	48.260	0.590	21.554	1.835	0.001
VV/VH	3.737	14.965	57.444	0.325	3.871	0.116	18.446	1.093	0.000

Algorithm calibrations

From a series of five automatic learning algorithms, the idea was to select the classifier that meets two conditions: (i) high overall accuracy and (ii) best performance in predicting the forest and cropland categories within the validation data.

The bias and variance of the calibration of the classifiers had notable differences with CV and MCCV (Fig. 6). That is, calibrations with CV had a slightly greater variance than calibrations with MCCV, mainly because CV only explores some of the possible ways in which data could have been partitioned (e.g., testing and training). In fact, MCCV allowed 90 times more exploration of possible partitions from a total of $C_{560}^{280} \approx \infty$. In short, the calibrations indicated that the algorithms with the best performance in overall accuracy and the lowest variance were SVM, NN, and RF (overall average accuracy of 97.50% and 98.00% with CV and MCCV respectively) for 2009 and NN (overall average accuracy of 93.93% and 94.80% with CV and MCCV respectively) for 2018 (Fig. 6). However, all classifiers had an acceptable overall accuracy greater than 90%. In both periods, the classifier with the lowest overall average accuracy was DT.

Fig. 6. The calibrations were performed through CV and MCCV, panel (a) is for the year 2009 and panel (b) is for the year 2018. The minimum, maximum and average of the overall accuracies for

each algorithm are shown. In addition, we show the variance obtained for the k=10 groups and for 100 iterations.

Table 4. Overall accuracy and Kappa index for all classification algorithms and both dates. Omission errors (OM) and commission errors (CO) are also shown. All values are in percentages (%). For overall accuracy, the highest values for each date are shown in bold, as well as lower commission and omission errors in the forest and cropland categories. The green background indicates the best classifier for each year, selected to maximize overall accuracy as well as minimize omission and commission errors for forest and cropland areas. See S2 in the supplementary material for more details.

		Overall Accuracy	Kappa Index	Water		Forest		Cropland		Bare soil	
				OM	CO	OM	CO	OM	CO	OM	CO
2009	SVM	95.09	93.07	0.00	0.00	0.00	9.00	22.22	2.78	2.44	2.44
	DT	93.30	90.55	2.13	0.00	1.10	10.0	26.67	8.33	2.44	4.76
	RF	**95.09**	93.11	2.13	0.00	1.10	**6.25**	**17.78**	5.13	2.44	6.98
	NB	93.30	90.58	2.13	0.00	2.20	9.18	24.44	10.53	2.44	4.76
	NN	95.09	93.09	0.00	0.00	**1.09**	8.16	20.00	5.26	2.44	2.44
2018	SVM	94.20	91.94	0.00	4.65	2.33	9.68	20.37	4.44	0.00	0.00
	DT	92.86	90.12	0.00	10.87	3.49	**6.74**	20.37	10.42	4.65	0.00
	RF	94.64	92.58	0.00	0.00	4.65	7.87	**12.96**	9.62	2.33	0.00
	NB	93.75	91.38	0.00	4.65	6.98	6.98	14.82	11.54	0.00	0.00
	NN	**95.09**	93.18	0.00	0.00	**2.33**	9.68	16.67	**4.25**	0.00	0.00

Visual examination of thematic maps

Since the objective is to quantify deforestation, it is very important that the algorithm optimally discriminates the forest from other types of cover. Fig. 7 and 8 show the thematic maps obtained by the five classifiers in 2009 and 2018 respectively. In both periods, especially in 2009, the visual interpretation between the thematic maps obtained by the five classifiers revealed an erroneous amount of the cropland class represented in the extreme north and southwest of the study area. In fact, a visual inspection of the Landsat images and high-resolution PlanetLabs images revealed that

these areas are predominantly covered by forests. However, there is also a certain level of deforestation in these areas, which could have led to confusion between forest and cropland classes. In general, all algorithms produced reasonably accurate land cover maps in both study periods. Nevertheless, the results of the RF algorithm in 2009 and NN in 2018 were of special interest as they show a better performance in separating forest and cropland cover with low omission and commission levels, and with an overall accuracy of 95.09% in both years (Table 4). A more detailed analysis showed that the average commission for the forest class in 2009 was 0.33% higher than in 2018, and the average omission for the same class in 2009 was 2.86% lower than in 2018. However, the "salt and pepper" effect was present in both periods, especially in 2018 for the classifiers NB, DT and NN (Fig. 7 and 8).

Fig. 7. Classifications using the six principal components of the fused image in the year 2009. Panels (a), (b), (c)*, (d) and (e) represent the classifications obtained with SVM, DT, RF (*the highest overall accuracy), NB and NN, respectively.

Fig. 8. Classifications using the five principal components of the fused image in the year 2018. Panels (a), (b), (c), (d) and (e)* represent the classifications obtained with SVM, DT, RF, NB, and NN (*the highest overall accuracy) respectively. Class "Difference*" represents the difference map of the same classifier between 2009 and 2018 with ground truth (Hansen et al., 2013).

Change validation and statistical comparisons

Fig. 9 shows deforestation areas obtained with the PVts-β approach, the RF-NN classifiers (i.e., changes obtained using the RF and NN classifiers) and the reference data. Visually, the detections of the PVts-β approach (Fig. 9a) and the RF-NN algorithms (Fig. 9b) reveal a lot of similarity with the reference data of Hansen et al. (2013) (Fig. 9c) and the MINAM reports (Fig. 9d), although a closer inspection showed some visual differences between the two detection methods, mainly south of the

study region (i.e., in elliptical white line). That is, a compact and continuous quantification should be expected. However, only the change obtained by the RF-NN classifiers shows something more detectable and logical (i.e., detection of deforestation in areas of gold activity should include not only the bare soil but also the water bodies in the areas).

However, the change maps showed that the overall accuracy obtained with the PVts-β approach was 92.91%. This was higher by 1.09% than the overall accuracy obtained with the RF-NN classifiers (Table 5). In addition, the lowest omissions and commissions were obtained with the PVts-β approach and RF-NN classifiers with 9.85% and 9.98% respectively. A visual analysis revealed that the commission of the PVts-β approach was mainly in gold mining areas, while the omission was in agricultural and gold mining areas, which were not optimally detected. Moreover, for a rigorous statistical comparative analysis, a forest/non-forest mask of the reference data from Hansen et al. (2013) was used to eliminate commissions from detection approaches. The statistics revealed that there was no significant difference between the mapped areas with respect to the reference data. In fact, both the PVts-β approach and the RF-NN algorithms detected a total of 18142.74ha and 16276.05ha respectively, while the reference data from Hansen et al. (2013) recorded 19708.35ha between 2009 and 2018. For the period 2009-2017 the PVts-β approach detected 15998.31ha, while Hansen et al. (2013) and MINAM reference data reported 16903.89ha and 17877.15ha respectively. Finally, from the changes obtained with the RF-NN classifiers, it is important to mention that between 2009 and 2018 the forests mainly changed to cropland 7169.49ha, bare soil 4507.56ha and water 4599.00ha.

Fig. 9. Panel (a) and (b) show deforestation detections (2009-2018) obtained from the PVts-β approach and the RF-NN classifiers respectively. Panel (c) and (d) show the reference data from Hansen et al. (2013) and MINAM respectively. All the panels have the SWIR1, NIR and RED combination from the year 2018 (Landsat 8 OLI) as the background.

Table 5. Overall accuracy, kappa index, and the average commission and omission errors (average commissions and omissions from deforestation classes and intact forest) are shown for the PVts-β approach, and for the change obtained with the RF-NN classifiers. All values are in percentages (%).

	Overall accuracy	Kappa index	Commission	Omission
PVts-β approach	92.91	78.36	11.67	9.85
Change with RF-NN	91.82	72.26	9.98	16.7

Discussion

As expected, image fusion showed that the HV and VH cross-polarizations had a slightly greater contribution than the HH and VV polarizations in PC1 (Table 3). In general, for the year 2009, it is observed that almost all the radar bands made a significant contribution to PC2:5, while for the year 2018, the highest radar contributions were observed in PC1:5 (except in PC4). In addition, the NIR band (a representative optical band for vegetation mapping) made a lower contribution than any other optical band in PC1 (even lower than the radar bands) in both study periods. However, this was not the case with the RED band. On the other hand, the vegetation structure (Shimada et al. 2014) and the detection of non-photosynthetic activity (e.g. fallen leaves) due to the penetration of ALOS PALSAR images, probably made it possible to map the forest class optimally in 2009 (see omission in Table 4).

To explore the performance of image fusion in detections, we detected changes only with optical images. These detections were underestimated by 2660ha with respect to the fused images, which is shown in S3 in the supplementary material. We believe that the difference between what is detected

with fused images and optical images is relatively small but it is an indicator that the fusion of optical and radar data contributes to the mapping of deforestation.

Fig. 10. Column (a) shows SAR images without a speckle filter, column (b) images with SSF, column (c) shows a Multi-temporal Speckle Filter (MSF). To evaluate the reduction of speckle noise we used three indicators: (i) visual interpretation, (ii) Signal Level Ratio (SLR) (White et al. 2020), and (iii) the standard deviation of the intensity before and after applying filters for areas with higher signal echo intensity (P3) and areas with lower signal echo intensity (P4) (column d). The parameters for the MSF filter were used by default: i) filter: filter Lee, ii) Number of looks: 1, iii) Window size: 7x7, and iv) Sigma: 0.9.

To analyse whether speckle noise and feature resolution had any influence on change detection, we decided to apply a Multi-temporal Speckle Filter (MSF) (Quegan and Yu 2001) to the SAR images before fusing with the optical data. For the year 2009, we obtained HH, HV and HH/HV polarizations from a total of 7 ALOS PALSAR images; while for the year 2018, we obtained VV, VH and VV/VH polarizations from a total of 11 S1B images (see S4 in the Supplementary material). The change map showed a deforestation of 16132.77ha between 2009 and 2018 (in both periods, we used PC1:6 ≈99% of cumulative variance) using the algorithms that performed best in the calibrations, i.e. RF in 2009 as well as 2018. Although MSF resulted in sharper and clearer boundaries (Fig. 10a-b-c in yellow and red lines), SSF together with optical data quantified the deforestation better. Similar results were obtained in the study by Mirelva and Nagasawa (2017) (although these authors only worked with radar data). Overall, no substantial differences were found between the two filter types (Fig. 10-P3, P4, Table 6), although for the areas with higher signal echo intensity the SSF filter performed better. In addition, the MSF seems to have an effect on the contribution of the SAR bands to the first PC, since lower contributions were observed with respect to SAR bands with SSF (see Table 3 and S4 for more details).

Table 6. SLR is a ratio of the unfiltered image to the filtered image averaged over a region (R1 and R2). A mean of one indicates that the filtered image preserves the signal level accurately. If the mean varies from one, then there is a bias in the filtering method.

		Mean			SLR	
		RAW	SSF	MSF	SSF	MSF
R1	HH	0.2139	0.2140	0.2130	0.9995	1.0042
	HV	0.0642	0.0642	0.0640	1.0000	1.0031
R2	VV	0.1417	0.1414	0.1774	1.0021	0.7988
	VH	0.0331	0.0331	0.0390	1.0000	0.8487

Although the classifications obtained with the five classifiers performed well in overall accuracy, they all had confusions between forest and cropland. This is mainly due to the similarity of the spectral response of the two coverages, predominantly in the optical electromagnetic spectrum. In these situations an increase in the number of variables, e.g. vegetation indices or other images from different dates, improves the separability of certain relatively confusing covers and slightly improves the overall accuracy of the classification, but does not detect deforestation better, as can be seen in section S5 on the supplementary material.

Another aspect that needs to be discussed is the presence of "salt and pepper" in all the classifications obtained, although much less in the period 2009. In general, SVM revealed a lower proportion of this type of noise in the two study periods. It is not clear whether the speckle noise of the SAR images was the main origin of the "salt and pepper" since Duro et al. (2012), who analysed optical images, also obtained similar results to ours with classifications contaminated by this type of noise in several algorithms of machine learning, although in a smaller proportion, by classifiers like SVM and RF. In addition, the study area is a region with very particular characteristics and it is a challenge to map deforestation, since the areas deforested by gold mining trigger not only the

presence of bare soil (i.e., sand), but also water bodies (Fig. 1c). This is a product of the activity itself which hinders certain pre-processing methods such as masking of atmospheric noise in optical images (Tarazona et al. 2018). That is, masking of atmospheric noise could mask areas that are deforested by mining activity. Therefore, the quantification of deforestation would reveal a certain degree of omission. This is clearly seen in the quantifications (yellow lines) carried out with the PVts-β approach and the reference data, but not so much with the quantifications carried out with the RF-NN classifiers (see Fig. 9). This difficulty is not present in the SAR images (this can be seen in the detection of fusion), where water bodies resulting from gold mining are recorded with low backscatter values (see white lines in Fig. 9b).

Another important point of discussion is the detection threshold of the PVts-β approach, since the omission of the detections occurred mainly in agricultural coverages. To avoid this deficiency, it is possible to lower the threshold to β=3; however, this could trigger a slight increase in the commission. In any case, for future work it will be important to assess to what extent a threshold of β=3 can increase commission levels, although the latter is possible to combat with a forest/non-forest mask.

Finally, according to this work's context, it is important to make an analysis of the detection approaches based on time series and those based on machine learning. Each approach has advantages and disadvantages in certain aspects. For example, it is clear that a machine learning approach, in contrast to a time series approach, is unlikely to detect slight changes over time in photosynthetic activity. However, if the atmospheric noise and seasonality of the time series are not eliminated or minimized correctly, it could make any further analysis in the time series difficult. On the other hand, the machine learning approach has the advantage from a computational and execution point of view (see S6 in the supplementary material). Furthermore, the main global deforestation mapping methodologies are based on classifications such as Hansen et al. (2013),

27

Hansen et al. (2016) and Asner et al. 2009 (CLASlite), although lately, thanks to the GEE platform (Gorelick et al. 2017), there have been efforts to implement detections based on time series, such as the LandTrendr method (Kennedy et al. 2010), which is embedded in GEE (https://emapr.github.io/LT-GEE/). However, most detection methods based on time series have: i) excessive calibration parameters, ii) are based strongly on seasonality, and iii) are complex to execute for a standard user. On the other hand, the PVts-β approach is a method that: i) is simple and intuitive and which does not model seasonality, ii) has only one calibration parameter to detect deforestation, and iii) can be easily implemented by any standard user.

Conclusions

Fusing optical and SAR data has been studied at length in the past, but the contribution (%) of each of the original variables within the fusion has not been addressed optimally. This research shows the benefits of combining optical and SAR data for detecting deforestation compared to using only optical data. The contribution of SAR bands, especially HV, HH/HV, VH and VV, was substantially important in both study periods. We believe that the benefits can be greater if the SAR images have been acquired after the optical images, since in areas of high precipitation cloud free optical images are usually only available between June and September. Therefore, when only optical images are used there is a void of three months with no record of the changes in the forest. Regarding speckle noise, although MSF better preserves the characteristics of the entities (better "spatial resolution"), it seems to decrease the contributions (unlike SSF) of the SAR bands in the data fusion and underestimates the detection of deforestation. In addition, there were no significant differences between the backscatter values obtained after applying MSF and SSF filters. However, the calibration of the machine learning algorithms revealed that all classifiers had an acceptable overall accuracy. In fact, all classifications had an overall accuracy of more than 90%.

The overall accuracy of the PVts-β and RF-NN detections were very similar, although the highest commission and lowest omission were obtained with the PVts-β approach. We believe that this

approach is a simple and intuitive detection method. Moreover, it can be applied to images that come from different sensors with dissimilar periodicity because it does not depend on the seasonality of the data (i.e., correlated data). In addition, it is important that the data set is large enough (> 5 data) to avoid bias in the calculation of the mean and standard deviation.

Finally, given the increased interest and activity in simple, effective and low-cost forest monitoring methods, PVts-β is clearly a strategic tool. Therefore, the PVts-β approach, the algorithm for fusing optical and radar data and other functions are implemented in an open source package called "ForesToolboxRS" (see Appendix B for more details).

Disclosure statement

The authors report that there is no conflict of interest .

ORCID

Yonatan Tarazona Coronel: 0000-0002-5208-1004

Alaitz Zabala: 0000-0002-3931-4221

Xavier Pons: 0000-0002-6924-1641

Antoni Broquetas: 0000-0001-9801-9145

Jakub Nowosad: 0000-0002-1057-3721

Hamdi A. Zurqani: 0000-0002-9250-4534

Appendix A.

All the variables (optical and SAR) are centred and scaled, and it is a question of calculating a new

set of bands $(Y_1, Y_2,\ldots, Y_p)$ uncorrelated among themselves, whose variances progressively

decrease. Each component Y_j $(j = 1, \ldots, p)$ is a linear combination of the original variables:

$$Y_1 = u_{11}Z_{1i} + u_{12}Z_{2i} + \cdots + u_{1p}Z_{pi} \qquad (1)$$

In abbreviated notation we will say $Y_1 = Zu_1$

So the variance of the first component will be:

$$var(Y_1) = \tfrac{1}{n}\sum_{i=1}^{n} Y_{1i}^2 = \tfrac{1}{n}Y_1^t Y_1 \qquad (2)$$

Eq. (1) in (2)

$$\tfrac{1}{n}u_1^t Z^t Zu_1 = u_1^t \left[\tfrac{1}{n}Z^t Z\right] u_1 = u_1^t Ru_1 \qquad (3)$$

The expression $\tfrac{1}{n}Z^t Z$ is the matrix of correlations (R) on standardized variables (i.e., centered and

scaled) (Jolliffe 2002; James et al. 2013).

The first component Y_1 is obtained so that its variance is maximum, that is, it is about finding Y_1

maximizing $var(Y_1) = u_1^t Ru_1$ with the restriction $\sum_{j=1}^{p} u_1^t u_1 = 1$.

Since the objective is to maximize a function of several variables subject to a constraint and the

incognita being u_1 (the unknown vector that gives the optimal linear combination) we will apply the

Lagrange multiplier:

$$L(u_1) = u_1^t Ru_1 - \lambda\left(u_1^t u_1 - 1\right) \qquad (4)$$

and then $\frac{\partial L}{\partial u_1}$ (derive with respect to the incognita u_1) and equal to zero:

$$\frac{\partial L}{\partial u_1} = 2Ru_1 - 2R = 0 \Rightarrow (R - \lambda I)u_1 = 0 \qquad (5)$$

Eq. 5 can be deduced that $|R - \lambda I| = 0$ and with roots $\lambda_1, \lambda_2, ..., \lambda_n$, ordered from highest to lowest $\lambda_1 > \lambda_2 > ... > \lambda_n$. On the other hand, if we multiply to the left by u_1^t, we conclude that:

$$u_1^t(R - \lambda I)u_1 = 0 \;\; \Rightarrow \;\; u_1^t R u_1 = \lambda \;\; \Rightarrow \;\; var\left(Y_1\right) = u_1^t R u_1 = \lambda$$

To maximize the variance of Y_1, we have to take the largest eigenvalues λ_1 and the corresponding eigenvectors u_1, so that the first component is defined as $Y_1 = Zu_1$. Therefore, all components are expressed as the product of the matrix of eigenvectors multiplied by the vector Z containing the original variables:

$$Y = uZ$$

Being,

$$Y = \left(Y_1 \, Y_2 \vdots Y_p\right) \quad u = \left(u_{11} \, u_{12} \cdots u_{1p} \, u_{21} \, u_{22} \cdots u_{2p} \cdots \cdots \cdots \cdots u_{p1} \, u_{p2} \cdots u_{pp}\right) \quad Z = \left(Z_1 \, Z_2 \vdots Z_p\right)$$

$$\text{and} \qquad \{var\left(Y_1\right) = \lambda_1 \; var\left(Y_2\right) = \lambda_2 \vdots var\left(Y_p\right) = \lambda_p$$

With the same logic it is possible to find the eigenvalues and eigenvectors for the remaining components.

Appendix B. Code

The source code and full instructions on how to execute the functions can be found through GitHub (please see https://github.com/ytarazona/ForesToolboxRS for more details).

References

Abdikan, S. 2016. "Exploring image fusion of ALOS/PALSAR data and LANDSAT data to differentiate forest area". *Geocarto International*, pp. 21-37. doi:10.1080/10106049.2016.1222635

Achard, F., Beuchle, R., Mayaux, P., Stibig, H.J., Bodart, C., Brink, A., Carboni, S., Desclée, B., Donnay, F., Eva, H.D., Lupi, A., Raši, R., Seliger, R., Simonetti, D. 2014. "Determination of tropical deforestation rates and related carbon losses from 1990 to 2010". *Global Change Biology*, Vol. 20: pp. 2540–2554. doi:10.1111/gcb.12605

Allnutt, T.F., Asner, G.P., Golden, C.D., Powell, G.V.N. 2013. "Mapping recent deforestation and forest disturbance in northeastern Madagascar". Trop. Conserv. Sci., Vol. 6(No. 1): pp. 1-15. doi:10.1177/194008291300600101

Asner, G.P, Knapp, D.E., Broadbent, E.N., Oliveira, P.J.C., Keller, M., Silva, J.N. 2005. "Selective logging in the Brazilian Amazon". Science, Vol. 5747: pp. 480–482. doi:10.1126/science.1118051

Asner, G.P., Knapp, D.E., Balaji, A., Paez-Acosta, G. 2009. "Automated mapping of tropical deforestation and forest degradation: CLASlite". J. Appl. Remote Sens, Vol. 3(No. 1): pp. 033543. doi:10.1117/1.3223675

Baccini, A., Goetz, S.J., Walker, W.S., Laporte, N.T., Sun, M., Sulla-Menashe, D., Hackler, J., Beck, P.S.A., Dubayah, R., Friedl, M.A., Samanta, S., Houghton, R.A. 2012. "Estimated carbon dioxide emissions from tropical deforestation improved by carbondensity maps". Nat. Clim. Change, Vol. 2: pp. 1-4. doi:10.1038/nclimate1354

Belgiu, M., Drăguţ., L. 2016. "Random Forest in Remote Sensing: A Review of Applications and Future Directions". ISPRS Journal of Photogrammetry and Remote Sensing, Vol. 114: pp. 24-31. doi:10.1016/j.isprsjprs.2016.01.011

Bryan, J.E., Shearman, P.L., Asner, G.P., Knapp, D.E., Aoro, G., Lokes, B. 2013. "Extreme differences in forest degradation in Borneo: comparing practices in Sarawak, Sabah, and Brunei". PLoS One, Vol. 8(No. 7). doi:10.1371/journal.pone.0069679

Carlson, K.M., Curran, L.M., Ratnasari, D., Pittman, A.M., Soares-Filho, B.S., Asner, G.P., Trigg, S.N., Gaveau, D.A., Lawrence, D., Rodrigues, H.O. 2012. "Committed carbon emissions, deforestation, and community land conversion from oil palm plantation expansion in West Kalimantan, Indonesia". Proc. Natl. Acad. Sci. U.S.A., Vol. 109(No. 19): pp. 7559–7564. doi:10.1073/pnas.1200452109

Chen, Y., Niu, Z., Johnston, C.A., Hu, S. 2019. "A Unifying Approach to Classifying Wetlands in the Ontonagon River Basin, Michigan, Using Multi-temporal Landsat-8 OLI Imagery". Canadian Journal of Remote Sensing, Vol. 44: pp. 373-389. doi:10.1080/07038992.2018.1526065

Congalton, R.G., Green, K. 2008. Assessing the Accuracy of Remotely Sensed Data, Principles and Practices. CRC Press.

Ding, Y., Zang, R., Lu, X., Huang, J. 2019. "Functional features of tropical montane rain forests along a logging intensity". Ecological Indicators, Vol. 97: pp. 311-318. doi:10.1016/j.ecolind.2018.10.030

Dlamini, W.M. 2017. "Mapping forest and woodland loss in Swaziland: 1990–2015". Remote Sens. Appl.: Soc. Environ., Vol. 5: pp. 45-53. doi:10.1016/j.rsase.2017.01.004

Duro, D.C., Franklin, S.E., Dubé, M.G. 2012. "A comparison of pixel-based and object-based image analysis with selected machine learning algorithms for the classification of agricultural landscapes using SPOT-5 HRG imagery". Remote Sensing of Environment, Vol. 118: pp. 259–272. doi:10.1016/j.rse.2011.11.020

FAO. 2018. "Global Forest Resources Assessment 2020". Rome, Italy. doi:http://www.fao.org/3/I8661EN/i8661en.pdf

Friedl, M. A., and C. E. Brodley. 1997. "Decision Tree Classification of Land Cover Form Remotely Sensed Data". Remote Sensing of Environment, Vol. 61: pp. 399–409. doi:10.1016/S0034-4257(97)00049-7

Frison, P.-L., Fruneau, B., Kmiha, S., Soudani, K., Dufrêne, E., Le Toan, T., Koleck, T., Villard, L., Mougin, E., Rudant, J.-P. 2018. "Potential of Sentinel-1 Data for Monitoring Temperate Mixed Forest Phenology". remote sensing, Vol. 10(No. 12): pp. 2049. doi:10.3390/rs10122049

Gibson, L., Lee, T.M., Koh, L.P., Brook, B.W., Gardner, T.A., Barlow, J., Peres, C.A., Bradshaw, C.J.A., Laurance, W.F., Lovejoy, T.E., Sodhi, N.S. 2011. "Primary forests are irreplaceable for sustaining tropical biodiversity". Nature, Vol. 478: pp. 378–381. doi:10.1038/nature10425

Gorelick, N., Hancher, M., Dixon, M., Ilyushchenko, S., Thau, D., Moore, R. 2017. "Google Earth Engine: Planetary-scale geospatial analysis for everyone". Remote Sensing of Environment, Vol. 202: pp. 18-27. doi:10.1016/j.rse.2017.06.031

Hansen, M.C., Krylov, A., Tyukavina, A., Potapov, P.V., Turubanova, S., Zutta, B., Ifo, S., Margono, B., Stolle, F., Moore, R. 2016. "Humid tropical forest disturbance alerts using

Landsat data". Environmental Research Letters, Vol. 11: pp. 034008. doi:10.1088/1748-9326/11/3/034008

Hansen, M.C., Potapov, P.V., Moore, R., Hancher, M., Turubanova, S.A., Tyukavina, A., Thau, D., Stehman, S.V., Goetz, S.J., Loveland, T.R., Kommareddy, A., Egorov, A., Chini, L., Justice, C.O., Townshend, J.R.G. 2013. "High Resolution Global Maps of 21st-Century Forest Cover Change". Science, Vol. 342: pp. 850–853. doi:10.1126/science.1244693

Hansen, M.C., Stehman, S.V., Potapov, P.V., Loveland, T.R., Townshend, J.R.G., DeFries, R.S., Pittman, K.W., Arunarwati, B., Stolle, F., Steininger, M.K., Carroll, M., DiMiceli, C. 2008. "Humid tropical forest clearing from 2000 to 2005 quantified by using multitemporal and multiresolution remotely sensed data". PNAS, Vol. 105: pp. 9439–9444. doi:10.1073/pnas.0804042105

He, Y., Lee, E., Warner, T.A. 2017. "A Time Series of Annual Land Use and Land Cover Maps of China from 1982 to 2013 Generated Using AVHRR GIMMS NDVI3g Data". Remote Sensing of Environment, Vol. 199: pp. 201-217. doi:10.1016/j.rse.2017.07.010

Hong, G., Zhang, Y. 2008. "Comparison and improvement of wavelet-based image fusion". International Journal of Remote Sensing, Vol. 29(No. 3): pp. 673-691. doi:10.1080/01431160701313826

Houghton, R. A. 2013. "The emissions of carbon from deforestation and degradation in the tropics: past trends and future potentia". Carbon Manage, Vol. 4: pp. 539–46. doi:10.4155/cmt.13.41

Imangholiloo, M., Rasinmäki, J., Rauste, Y., Holopainen, M. 2020. "Delineation of Bare Soil Field Areas from Unmanned "Aircraft System Imagery with the Mean Shift Unsupervised Clustering and the Random Forest Supervised Classification". Canadian Journal of Remote Sensing, Vol. 45: pp. 489-500. doi:10.1080/07038992.2019.1635877

Imangholiloo, M., Rasinmäki, J., Rauste, Y., Holopainen, M. 2020. "Delineation of Bare Soil Field Areas from Unmanned "Aircraft System Imagery with the Mean Shift Unsupervised Clustering and the Random Forest Supervised Classification". Canadian Journal of Remote Sensing, Vol. 46: pp. 489-500. doi: 10.1080/07038992.2020.1763789

James, G., Witten, D., Hastie, T., Tibshirani, R. 2013. An Introduction to Statistical Learning - with Applications in R. New York: Springer.

Jia, M., Lei Wang, L. 2018. "Novel class-relativity non-local means with principal component analysis for multitemporal SAR image change detection". International Journal of Remote Sensing, Vol.39 (No. 4): pp. 1068-1091. doi:10.1080/01431161.2017.1395966

Jolliffe, I.T. 2002. Principal Component Analysis (Second Edition ed.). Springer. doi:10.1007/b98835

Joshi, N., Baumann, M., Ehammer, A., Fensholt, R., Grogan, K., Hostert, P., Jepsen, M.R., Kuemmerle, T., Meyfroidt, P., Mitchard, E.T.A., Reiche, J., Ryan, C.M., Waske, B. 2016. "A review of the application of optical and radar remote sensing data fusion to land use mapping and monitoring". Remote Sens., Vol. 8(No. 1), pp. 70. doi:10.3390/rs8010070

Kennedy, R.E., Yang, Z., Cohen, W.B. 2010. "Detecting trends in forest disturbance and recovery using yearly Landsat time series: 1. LandTrendr — temporal segmentation". Remote Sensing of Environment, Vol. 114(No. 12): pp. 2897–2910. doi:10.1016/j.rse.2010.07.008

Knorn, J., Rabe, A., Radeloff, V.C., Kuemmerle, T., Kozak, J., Hostert, P. 2009. "Land cover mapping of large areas using chain classification of neighboring Landsat satellite images". Remote Sensing of Environment, Vol. 113(No. 5): pp. 957–964. doi:10.1016/j.rse.2009.01.010

Lee, J. S. 1980. "Digital image enhancement and noise filtering by use of local statistics". IEEE Trans, on Pattern Analysis and Machine Intelligence, Vol. 2(No. 2): pp. 165-168. doi:10.1109/TPAMI.1980.4766994

Liu, X., Wang, C., Meng, Y., Wang, H., Fu, M., Bourennane, S. 2019. "Target Detection Based on Spectral Derivation in HSI Shadow Region Classified by Convolutional Neural Networks". Canadian Journal of Remote Sensing, Vol. 45: pp. 782-794. doi:10.1080/07038992.2019.1697221

Lu, D., Li, G., Moran, E., Batistella, M., Freitas, C.C. 2011. "Mapping impervious surfaces with the integrated use of Landsat Thematic Mapper and radar data: A case study in an urban–rural landscape in the Brazilian Amazon". ISPRS Journal of Photogrammetry and Remote Sensing, Vol. 66: pp. 798-808. doi:10.1016/j.isprsjprs.2011.08.004

MINAM. 2015. "Protocolo de clasificación de Pérdida de Cobertura en los Bosques Húmedos Amazónicos entre los años 2000–2011. Resolución Ministerial Perú, Lima". doi:http://www.bosques.gob.pe/archivo/files/pdf/protocolo_

Mirelva, P.R., and Nagasawa, R. 2017. "Single and multitemporal filtering comparison on synthetic aperture radar data for agriculture area classification". Paper presented at ICISPC 2017: Proceedings of the International Conference on Imaging, Signal Processing and Communication, Penang, Penang, July. doi:10.1145/3132300.3132316

Mountrakis, G., Im, J., Ogole, C. 2011. "Support vector machines in remote sensing: A review". ISPRS Journal of Photogrammetry and Remote Sensing, Vol. 66: pp. 247–259. doi:10.1016/j.isprsjprs.2010.11.001

Olofsson, P., Foody, G.M., Herold, M., Stehman, S.V., Woodcock, C.E., Wulder, M.A. 2014. "Good practices for estimating area and assessing accuracy of land change". Remote Sensing of Environment, Vol. 148: pp. 42-57. doi:10.1016/j.rse.2014.02.015

Pal, M. 2005. "Random Forest Classifier for Remote Sensing Classification". International Journal of Remote Sensing, Vol. 26(No. 1): pp. 217–222. doi:10.1080/01431160412331269698

Park, N.W., Chi, K.H. 2008. "Integration of multitemporal/polarization C‑band SAR data sets for land‑cover classification". International Journal of Remote Sensing, Vol. 29(No. 16): pp. 4667-4688. doi:10.1080/01431160801947341

Pereira, L.O., Freitas, C.C., Anna, S.J.S.S., Lu, D., Moran, E.F. 2013. "Optical and radar data integration for land use and land cover mapping in the Brazilian Amazon". GIScience & Remote Sensing, Vol. 50(No. 3): pp. 301-321. doi:10.1080/15481603.2013.805589

Pôssa, E.M., Maillard, P. 2018. "Precise Delineation of Small Water Bodies from Sentinel-1 Data using Support Vector Machine Classification". Canadian Journal of Remote Sensing, Vol. 44: pp. 179-190. doi:10.1080/07038992.2018.1478723

Potapov, P., Turubanova, S., Hansen, M.C. 2011. "Regional scale boreal forest cover and change mapping using landsat data composites for European Russia". Remote Sens. Environ., Vol. 115(No. 2): pp. 548–561. doi:10.1016/j.rse.2010.10.001

Pradhan, R., Ghose, M.K., Jeyaram, A. 2010. "Land Cover Classification of Remotely Sensed Satellite Data using Bayesian and Hybrid classifier". International Journal of Computer Applications, Vol. 7(No. 11). doi:10.5120/1295-1783

Quegan, S., Yu., J.J. 2001. "Filtering of Multichannel SAR Images". IEEE Transactions on Geoscience and Remote Sensing, Vol. 39(No. 11): pp. 2373-2379. doi:10.1109/36.964973

R Core Team. 2020. "R: A language and environment for statistical computing". R Foundation for Statistical Computing, Vienna, Austria. doi:https://www.R-project.org/

Reiche, J., Hamunyela, E., Verbesselt, J., Hoekman, D., Herold, M. 2018. "Improving near-real time deforestation monitoring in tropical dry forests by combining dense Sentinel-1 time series with Landsat and ALOS-2 PALSAR-2". Remote Sensing of Environment, Vol. 204: pp. 147-161. doi:10.1016/j.rse.2017.10.034

Rodriguez-Galiano, V.F., Ghimire, B., Rogan, J., Chica-Olmo, M., Rigol-Sanchez, J.P. 2012. "An Assessment of the Effectiveness of a Random Forest Classifier for Land-Cover

Classification". ISPRS Journal of Photogrammetry and Remote Sensing, Vol. 67: pp. 93-104. doi:10.1016/j.isprsjprs.2011.11.002

Rosenqvist, A., Shimada, M., Ito, N., Watanabe, M. 2007. "ALOS PALSAR: a pathfinder mission for global-scale monitoring of the environment". IEEE Trans. Geosci. Remote Sens., Vol. 45: pp. 3307–3316. doi:10.1109/TGRS.2007.901027

Schultz, M., Clevers, J.G.P.W., Carter, S., Verbesselt, J., Avitabile, V., Quang, H.V., Herold, M. 2016. "Performance of vegetation indices from Landsat time series in deforestation monitoring". Int. J. Appl. Earth Obs. Geoinf., Vol. 52: pp. 318–327. doi:10.1016/j.jag.2016.06.020

Shimada, M., Itoh, T., Motooka, T., Watanabe, M., Shiraishi , T., Thapa, R., Lucas, R. 2014. "New global forest/non-forest maps from ALOS PALSAR data (2007–2010)". Remote Sensing of Environment, Vol. 155: pp. 13-31. doi:10.1016/j.rse.2014.04.014

Souza, C., Roberts, D.A., Cochrane, M.A. 2005. "Combining spectral and spatial information to map canopy damage from selective logging and forest fires". Remote Sensing of Environment, Vol. 98: pp. 329 – 343. doi:10.1016/j.rse.2005.07.013

Souza, C.M., Siqueira, J.V., Sales, M.H., Fonseca, A.V., Ribeiro, J.G., Numata, I., Cochrane, M.A., Barber, C.P., Roberts, D.A., Barlow, J. 2013. "Ten-year landsat classification of deforestation and forest degradation in the Brazilian Amazon". Remote Sensing, Vol. 5: pp. 5493–5513. doi:10.3390/rs5115493

Tarazona, Y., Mantas, V.M., Pereira, A.J.S.C. 2018. "Improving tropical deforestation detection through using photosynthetic vegetation time series – (PVts-β)". Ecological Indicators, Vol. 94: pp. 367–379. doi:10.1016/j.ecolind.2018.07.012

Tarazona, Y., Miyasiro-López, M. 2020. "Monitoring tropical forest degradation using remote sensing. Challenges and opportunities in the Madre de Dios region, Peru". Remote Sensing Applications: Society and Environment, Vol. 19: pp. 100337. doi:10.1016/j.rsase.2020.100337

Tibshirani, R., Walther, G., Hastie, T. 2001. "Estimating the number of clusters in a data set via the gap statistic". Royal Statistical Society, pp. 411-423. doi:10.1111/1467-9868.00293

Torres, R., Snoeij, P., Geudtner, D., Bibby, D., Davidson, M., Attema, E., Potin, P., Rommen, B., Floury, N., Brown, M., Traver, I.N., Deghaye, P., Duesmann, B., Rosich, B., Miranda, N., Bruno, C., L'Abbate, M., Croci, R., Pietropaolo, A., Huchler, M., Ro. 2012. "GMES Sentinel-1 mission". Remote Sens. Environ., Vol. 120: pp. 9-24. doi:10.1016/j.rse.2011.05.028

Trisasongko, B.H. 2010. "The use of polarimetric SAR data for forest disturbance monitoring". Sens. Imaging, Vol. 11: pp. 1-13. doi:10.1007/s11220-010-0048-8

Turubanova, S., Potapov, P.V., Tyukavina, A., Hansen, M.C. 2018. "Ongoing primary forest loss in Brazil, Democratic Republic of the Congo, and Indonesia". Environmental Research Letters, Vol. 13: pp. 074028. doi:10.1088/1748-9326/aacd1c

Tyralis, H., Papacharalampous, G., Langousis, A. 2019. "A Brief Review of Random Forests for Water Scientists and Practitioners and Their Recent History in Water Resources". water, Vol. 11(No. 5): pp. 910. doi:10.3390/w11050910

van der Werf, G.R., Morton, D.C., DeFries, R.S., Olivier, J.G.J., Kasibhatla, P.S., Jackson, R.B., Collatz, G.J., Randerson, J.T. 2009. "CO2 emissions from forest loss". Nature Geoscience, Vol. 2: pp. 737–738. doi:10.1038/ngeo671

Verbesselt, J., Zeileis, A., Herold, M. 2012. "Near real-time disturbance detection using satellite image time series". Remote Sensing of Environment, Vol. 123: pp. 98-108. doi:10.1016/j.rse.2012.02.022

Vidal-Macua, J.J., Ninyerola, M., Zabala, A., Domingo-Marimon, C., Pons, X. 2017. "Factors affecting forest dynamics in the Iberian Peninsula from 1987 to 2012. The role of topography and drought". Forest Ecology and Management, Vol. 406: pp. 290-306. doi:10.1016/j.foreco.2017.10.011

Walker, W.S., Stickler, C.M., Kellndorfer, J.M., Kirsch, K.M., Nepstad, D.C. 2010. "Large area classification and mapping of forest and land cover in the Brazilian Amazon: A comparative analysis of ALOS/PALSAR and landsat data sources". IEEE Journal on Selected Topics in Applied Earth Observations and Remote Sensing, Vol. 3: pp. 594–604. doi:10.1109/JSTARS.2010.2076398

Werner, A., Storie, C.D., Storie, J. 2014. "Evaluating SAR-Optical Image Fusions for Urban LULC Classification in Vancouver Canada". Canadian Journal of Remote Sensing, Vol. 40: pp. 278-290. doi:10.1080/07038992.2014.976700

White, L., Brisco, B., Murnaghan, K., Pasher, J., Duffe, J. 2020. "Temporal Filters for Mapping Phragmites with C-HH SAR Data". Canadian Journal of Remote Sensing, Vol. 46(No. 3): pp. 376-385. doi:10.1080/07038992.2020.1799770

Woodhouse, I.H. 2005. Introduction to Microwave Remote Sensing. CRC Press.

Young, N.E., Anderson, R.S., Chignell, S.M., Vorster, A.G., Lawrence, R., Evangelista, P.H. 2017. "A survival guide to Landsat preprocessing". Ecology, Vol. 98(No. 4): pp. 920–932. doi:10.1002/ecy.1730

Zeng, T., Dong, X., Quegan, S., Hu, C., Uryu, Y. 2014. "Regional tropical deforestation detection using ALOS PALSAR 50 m mosaics in Riau province, Indonesia". Electronics Letters, Vol. 50(No. 7): pp. 547–549. doi:10.1049/el.2013.4254

Zhang, J. 2010. "Multi-source remote sensing data fusion: status and trends". International Journal of Image and Data Fusion, Vol. 1: pp. 5-24. doi:10.1080/19479830903561035

Zhu, Z., Woodcock, C.E. 2012. "Object-based cloud and cloud shadow detection in Landsat imagery". Remote Sens. Environ, Vol. 118: pp. 83-94. doi:10.1016/j.rse.2011.10.028

Zhu, Z., Woodcock, C.E. 2014. "Continuous change detection and classification of land cover using all available Landsat data". Remote Sensing of Environment, Vol. 144: pp. 152–171. doi:10.1016/j.rse.2014.01.011

Zhu, Z., Wulder, M.A., Roy, D.P., Woodcock, C.E., Hansen, M.C., Radeloff, V.C., Healey, S.P., Schaaf, C., Hostert, P., Strobl, P., Pekel, J.F., Lymburner, L., Pahlevan, N., Scambos, T.A. 2019. "Benefits of the free and open Landsat data policy". Remote Sensing of Environment, Vol. 224: pp. 382–385. doi:10.1016/j.rse.2019.02.016

Zurqani, H.A., Post, C.J., Mikhailova, E.A., Allen, J.S. 2019. "Mapping Urbanization Trends in a Forested Landscape Using Google Earth Engine". Remote Sensing in Earth Systems Sciences, pp. 1-10. doi:10.1007/s41976-019-00020-y

Supplementary material

S1:

Important packages and parameters used in each classifier.

Classifier	Important parameters	Package
SVM	Kernel= linear	e1071
DT	method = "anova", type="class"	rpart
RF	ntree=500, mtry=$\sqrt{n}$, n: samples importance=TRUE	randomForest
NB	laplace = 0	e1071
NN	Weights=1, size=50, rang=0.1, decay=5e-4, maxit=200, trace=FALSE	nnet

S2: Green background indicates the best classifier for each year, selected to maximize overall accuracy as well as to minimize omission and commission errors for forests.

	2009															
	Support Vector Machine									**Naive Bayes**						
	Reference									**Reference**						
Prediction	Water	Forest	Cropland	Soil	Total	UA	CO		**Prediction**	Water	Forest	Cropland	soil	Total	UA	CO
Water	47	0	0	0	47	100	0.00		Water	46	0	0	0	46	100	0.00
Forest	0	91	9	0	100	91.00	9.00		Forest	0	89	9	0	98	90.82	9.18
Cropland	0	0	35	1	36	97.22	2.78		Cropland	1	2	34	1	38	89.47	10.53
Soil	0	0	1	40	41	97.56	2.44		Soil	0	0	2	40	42	95.24	4.76
Total	47	91	45	41	224				Total	47	91	45	41	224		
PA	100	100	77.78	97.56		OA=95.09%			PA	97.87	97.80	75.56	97.56		OA=93.30%	
OM	0.00	0.00	22.22	2.44		Kappa=93.07%			OM	2.13	2.20	24.44	2.44		Kappa=90.58%	
	Decision Tree									**Neural Network**						
	Reference									**Reference**						
Prediction	Water	Forest	Cropland	Soil	Total	UA	CO		**Prediction**	Water	Forest	Cropland	Soil	Total	UA	CO
Water	46	0	0	0	46	100	0.00		Water	47	0	0	0	47	100	0.00
Forest	0	90	10	0	100	90.00	10.0		Forest	0	90	8	0	98	91.84	8.16
Cropland	1	1	33	1	36	91.67	8.33		Cropland	0	1	36	1	38	94.74	5.26
Soil	0	0	2	40	42	95.24	4.76		Soil	0	0	1	40	41	97.56	2.44
Total	47	91	45	41	224				Total	47	91	45	41	224		
PA	97.87	98.90	73.33	97.56		OA=93.30%			PA	100	98.90	80.00	97.56		OA=95.09%	
OM	2.13	1.10	26.67	2.44		Kappa=90.55%			OM	0.00	1.09	20.00	2.44		Kappa=93.09%	

Random Forest

Reference

Prediction	Water	Forest	Cropland	Soil	Total	UA	CO
Water	46	0	0	0	46	100	0.00
Forest	0	90	6	0	96	93.75	6.25
Cropland	0	1	37	1	39	94.87	5.13
Soil	1	0	2	40	43	93.02	6.98
Total	47	91	45	41	224		
PA	97.87	98.90	82.22	97.56		OA=95.09%	
OM	2.13	1.10	17.78	2.44		Kappa=93.11%	

2018

Support Vector Machine

Reference

Prediction	Water	Forest	Cropland	Soil	Total	UA	CO
Water	41	0	2	0	43	95.35	4.65
Forest	0	84	9	0	93	90.32	9.68
Cropland	0	2	43	0	45	95.56	4.44
Soil	0	0	0	43	43	100	0.00
Total	41	86	54	43	224		
PA	100	97.67	79.63	100		OA=94.20%	
OM	0.00	2.33	20.37	0.00		Kappa=91.94%	

Naive Bayes

Reference

Prediction	Water	Forest	Cropland	Soil	Total	UA	CO
Water	41	0	2	0	43	95.35	4.65
Forest	0	80	6	0	86	93.02	6.98
Cropland	0	6	46	0	52	88.46	11.54
Soil	0	0	0	43	43	100	0.00
Total	41	86	54	43	224		
PA	100	93.02	85.19	100		OA=93.75%	
OM	0.00	6.98	14.82	0.00		Kappa=91.38%	

Decision Tree

Reference

Prediction	Water	Forest	Cropland	Soil	Total	UA	CO
Water	41	0	5	0	46	89.13	10.87
Forest	0	83	6	0	89	93.26	6.74
Cropland	0	3	43	2	48	89.58	10.42
Soil	0	0	0	41	41	100	0.00
Total	41	86	54	43	224		
PA	100	96.51	79.63	95.35		OA=92.86%	
OM	0.00	3.49	20.37	4.65		Kappa=90.12%	

Neural Network

Reference

Prediction	Water	Forest	Cropland	Soil	Total	UA	CO
Water	41	0	0	0	41	100	0.00
Forest	0	84	9	0	93	90.32	9.68
Cropland	0	2	45	0	47	95.75	4.25
Soil	0	0	0	43	43	100	0.00
Total	41	86	54	43	224		
PA	100	97.67	83.33	100		OA=95.09%	
OM	0.00	2.33	16.67	0.00		Kappa=93.18%	

Random Forest

Reference

Prediction	Water	Forest	Cropland	Soil	Total	UA	CO
Water	41	0	0	0	41	100	0.00
Forest	0	82	7	0	89	92.13	7.87
Cropland	0	4	47	1	52	90.38	9.62
Soil	0	0	0	42	42	100	0.00
Total	41	86	54	43	224		

PA	100	95.38	87.04	97.67		OA=94.64%						
OM	0.00	4.65	12.96	2.33		Kappa=92.58%						

S3:

To explore the performance of image fusion in detections, we detected changes only with optical images, using the DT classifier in 2009 and RF in 2018 (as were the ones with best performance in this case) giving a total of 15482.88ha of deforestation between 2009 and 2018. These statistics are below the changes detected with the PVts-β approach (18142.74ha) and the RF-NN classifiers on fused images (16276.05ha) for the same period. We believe that the difference between what is detected by fused images and optical images is relatively small but it is an indicator that the fusion of optical and radar data contributes to the mapping of deforestation.

Classifications using only optical images. The calibrations were performed through CV and MCCV, being panel (a) for the year 2009 and panel (b) for the year 2018. The minimum, maximum and average of the overall accuracies for each algorithm are shown. In addition, we show the variance obtained for the k=10 groups and for 100 iterations.
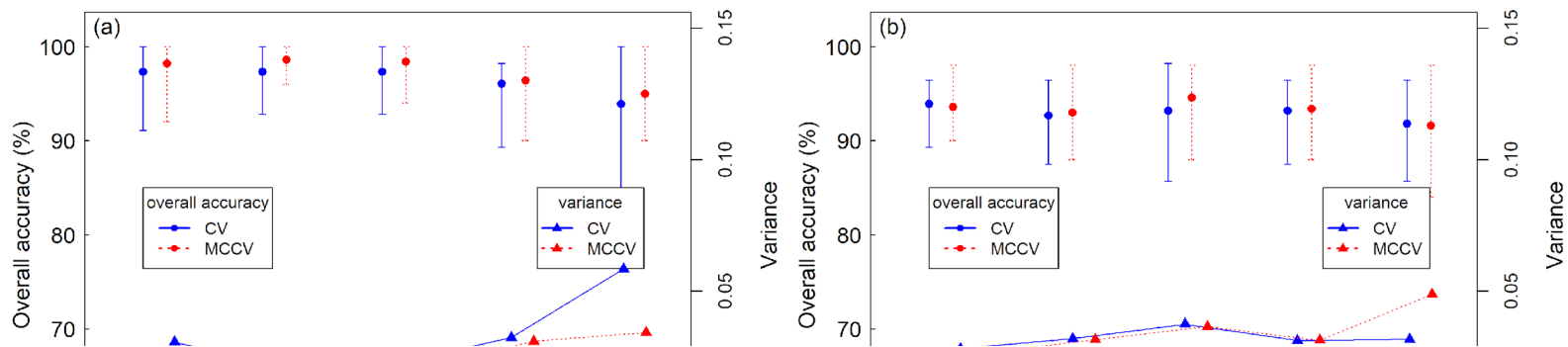
S4: The acquisition dates of the ALOS PALSAR and Sentinel 1B images used for the Multi-temporal Speckle Filter are shown.

N°	Date (Day/month/year)	
	ALOS PALSAR	Sentinel 1B
1		
2	22062007	12102018
3	07082007	23102018
4	09052008	04112018
5	24062008	05112018
6	09082008	16112018
7	27062009	17112018
8	12082009	28112018
9		29112018
10		10122018
11		11122018
12		22122018

Variance and the accumulation of variance for optical data fusion and Multi-temporal Speckle Filter SAR bands are shown.
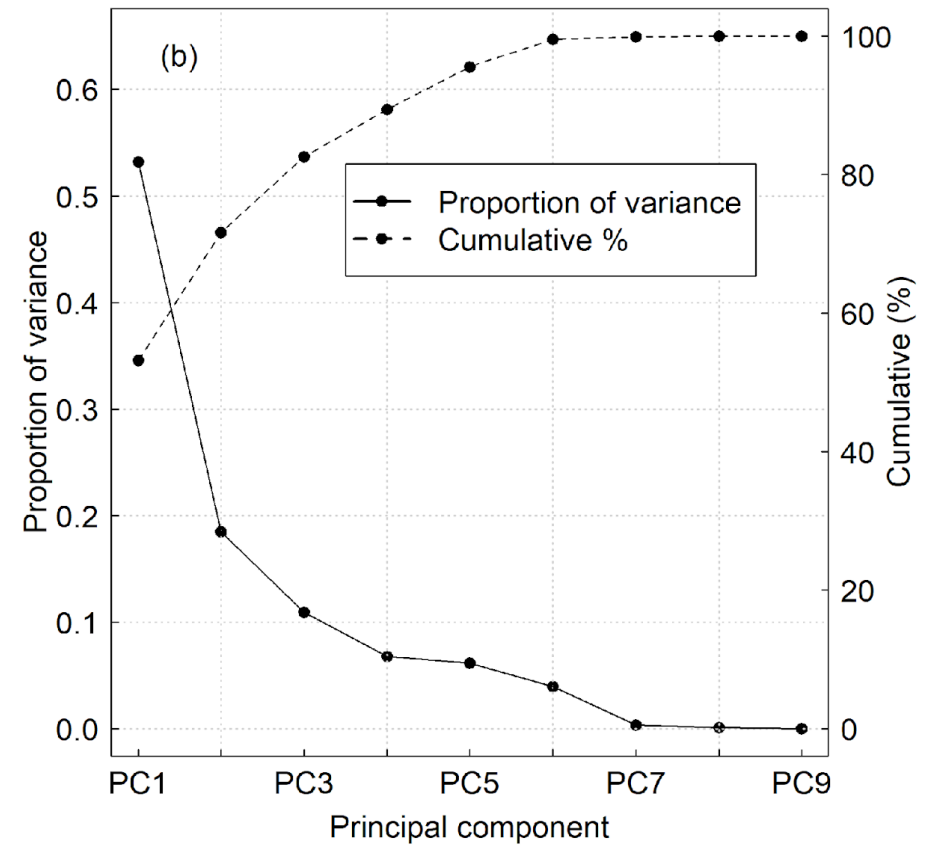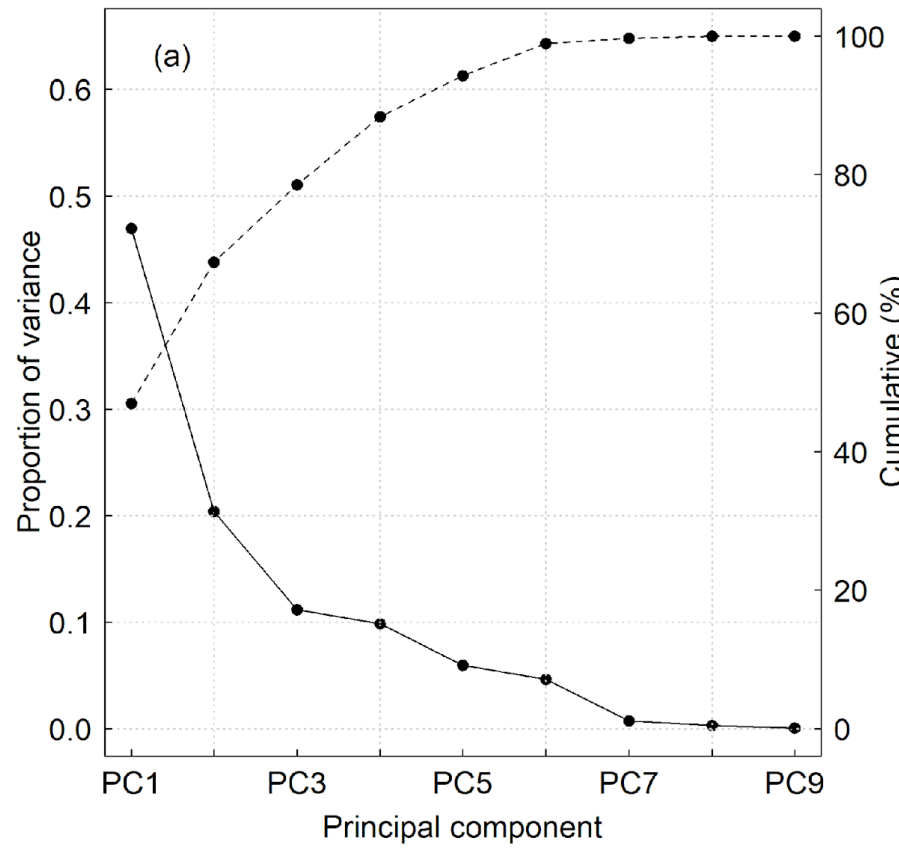
Correlations and contributions to optical and SAR data fusion with Multi-temporal Speckle Filter are shown.

Correlations									
Year 2009									
	PC1	PC2	PC3	PC4	PC5	PC6	PC7	PC8	PC9
BLUE	0.926	0.132	-0.031	0.191	-0.163	0.149	0.190	-0.000	0.015
GREEN	0.959	0.086	-0.030	0.180	-0.149	0.111	-0.040	-0.017	-0.044
RED	0.937	0.159	-0.049	0.221	-0.125	0.034	-0.158	-0.019	0.029
NIR	0.238	-0.780	0.165	-0.390	-0.093	0.376	-0.029	0.046	0.003
SWIR1	0.715	-0.548	0.104	-0.285	0.202	-0.204	0.025	-0.104	0.001
SWIR2	0.905	-0.150	0.018	-0.041	0.182	-0.330	0.002	0.109	-0.001
HH	-0.157	-0.611	-0.303	0.597	0.365	0.139	0.000	0.000	0.000
HV	-0.373	-0.689	-0.094	0.234	-0.501	-0.263	0.006	-0.000	0.000
HH/VH	0.118	0.049	-0.928	-0.345	-0.041	0.008	0.000	0.000	0.000
Year 2018									
	PC1	PC2	PC3	PC4	PC5	PC6	PC7	PC8	PC9
BLUE	0.935	0.028	-0.006	-0.321	0.009	-0.046	-0.132	0.000	-0.001
GREEN	0.955	-0.007	-0.008	-0.284	0.031	-0.046	0.027	0.011	0.004
RED	0.957	-0.046	-0.009	-0.243	0.068	-0.050	0.112	0.006	-0.002
NIR	-0.081	0.825	-0.012	-0.163	-0.521	0.111	0.015	-0.009	0.000
SWIR1	0.687	0.593	-0.046	0.396	0.110	-0.001	-0.011	0.057	0.000
SWIR2	0.860	0.372	-0.036	0.286	0.181	-0.020	0.002	-0.067	0.000
VV	-0.596	0.506	0.078	-0.284	0.458	0.301	0.001	0.000	0.000
VH	-0.693	0.479	0.036	-0.140	0.143	-0.496	0.003	-0.001	0.000
VV/VH	0.158	-0.006	0.985	0.047	-0.035	-0.006	-0.000	0.000	0.000
Contributions (%)									
Year 2009									
	PC1	PC2	PC3	PC4	PC5	PC6	PC7	PC8	PC9
BLUE	20.321	0.957	0.098	4.133	5.027	5.352	56.150	0.000	7.958
GREEN	21.777	0.407	0.089	3.679	4.157	2.984	2.482	1.203	63.216
RED	20.812	1.379	0.243	5.544	2.947	0.287	38.960	1.504	28.319
NIR	1.347	33.191	2.729	17.241	1.644	33.951	1.317	8.238	0.337
SWIR1	12.112	16.401	1.079	9.217	7.695	10.005	1.017	42.410	0.060
SWIR2	19.413	1.230	0.035	0.197	6.257	26.110	0.006	46.640	0.107
HH	0.590	20.356	9.133	40.276	24.989	4.650	0.000	0.001	0.000
HV	3.293	25.938	0.882	6.223	46.955	16.641	0.065	0.000	0.000
HH/HV	0.330	0.135	85.708	13.484	0.324	0.016	0.000	0.000	0.000
Year 2018									
	PC1	PC2	PC3	PC4	PC5	PC6	PC7	PC8	PC9
BLUE	18.291	0.047	0.004	16.861	0.015	0.615	55.856	0.000	8.306
GREEN	19.065	0.003	0.006	13.259	0.178	0.608	2.363	1.728	62.785
RED	19.161	0.132	0.008	9.702	0.849	0.712	40.557	0.474	28.401
NIR	0.137	41.016	0.015	4.361	49.019	3.502	0.740	1.186	0.019
SWIR1	9.874	21.196	0.215	25.681	2.185	0.000	-0.418	40.281	0.145
SWIR2	15.464	8.334	0.133	13.364	5.917	0.113	0.022	56.309	0.340
VV	7.427	15.409	0.620	13.180	37.922	25.420	0.012	0.002	0.000
VH	10.054	13.856	0.132	3.213	3.686	69.010	0.029	0.014	0.000
VV/VH	0.523	0.002	98.862	0.374	0.225	0.010	0.000	0.000	0.000

S5:

Without denaturing the objectives of this study, we did the exercise of classifying using the principal components obtained in the fusion (i.e., PC1:6 and PC1:5 in 2009 and 2018 respectively) and adding 4 NDVI indices in total (2 in each period), i.e. two indices come from the images used (see section 3.3), and the others were acquired on September 6, 2009 and June 18, 2018. The best

classifiers in this scenario were SVM in 2009 (with OA of 97.77%), and NB in 2018 (with OA of 96.64%) (See S5 in supplementary material). Moreover, the addition of the multi-temporal indices improved discrimination of forest cover and also of cropland (particularly in 2009), not so in the quantification of the deforestation of 14673.54ha between 2009 and 2018 below that detected with the fused image (16276.05ha) (i.e., PC without indexes and SAR bands with SSF) and even below the detections obtained with the optical images (15482.88ha). At this point of the situation, some explanations arise, e.g. the indexes added in the classifications were acquired with an earlier date than the images used in the classifications, so that this retrogression in time could contaminate the changes that occurred in the image with a more recent date. Additionally, a thorough analysis revealed that these new detections, with respect to the fused images and the PVts-β approach, were mainly at the edges of change; so the addition of new variables such as NDVI indices may have decreased the sensitivity of the detections. Therefore, it is important to highlight that improving the classification accuracy of certain coverages through the addition of new variables may have a negative impact on the detection of change, at least this study suggest it. Consequently it will be important to address this aspect in future work in greater detail.

Overall accuracy and Kappa index for all classification algorithms and both dates (principal components + 2 NDVI indices). Omission errors (OM) and commission errors (CO) are also shown. All values are in percentages (%). For overall accuracy higher values for each date are shown in bold, as well as lower commission and omission errors in Forest category.

		Overall Accuracy	Kappa Index	Water		Forest		Cropland		Soil	
				OM	CO	OM	CO	OM	CO	OM	CO
2009	SVM	97.77	96.90	0.00	0.00	1.15	2.27	7.27	1.92	0.00	4.44
	DT	91.07	87.61	7.69	2.70	4.60	6.74	18.18	11.76	6.97	14.89
	RF	97.32	96.28	2.56	0.00	1.15	2.27	7.27	1.92	0.00	6.52
	NB	96.42	95.05	2.56	2.56	1.15	5.49	10.91	2.00	0.00	2.27
	NN	97.77	96.91	0.00	0.00	3.45	1.18	3.64	5.35	0.00	2.27

	SVM	93.75	91.17	0.00	0.00	3.26	11.00	22.00	7.14	0.00	0.00
20	DT	90.63	86.70	2.63	0.00	4.35	13.73	28.00	16.28	4.55	0.00
18	RF	93.75	91.20	2.63	0.00	4.35	8.33	16.00	12.50	2.27	0.00
	NB	94.64	92.47	2.63	0.00	4.38	7.39	14.00	10.42	0.00	0.00
	NN	92.86	90.04	2.63	0.00	4.35	6.82	28.00	18.52	4.55	0.00

S6:

For a window system with 4 processor cores, 16 GB RAM and using parallel programming, the execution times of the machine learning classifiers was considerably shorter than the execution time of the PVts-β approach (Table 6).

Execution times (in seconds) of both the machine learning classifiers and the pvts function (i.e., PVts-β approach).

		Classifier/ Approach	Time (s)		
			Fused image (PC1:6, PC1:5)	Optical image (6 bands)	PC1:6, PC1:5+2NDVI (6 bands)
Year 2009		SVM	4.85	4.39	4.84
		RF	11.00	9.03	5.64
		NB	97.09	95.04	107.55
		DT	3.57	3.61	4.77
		NN	2.75	2.02	3.72
Year 2018		SVM	3.93	4.75	5.43
		RF	9.34	8.84	9.50
		NB	91.82	96.17	101.28
		DT	3.47	3.54	3.73
		NN	2.59	1.85	2.44
Year (2009 - 2018)	PVts-β	Function "smootH"	848.09		
		Function "pvts"	64.82		

*to see the "smootH" and "pvts" functions see Appendix B for more details.